Published in final edited form as:
Opt Express. 2009 March 2; 17(5): 4095–4111.

Volumetric retinal imaging with ultrahigh-resolution spectral-domain optical coherence tomography and adaptive optics using two broadband light sources◊

Barry Cense*, **Eric Koperda**, **Jeffrey M. Brown**, **Omer P. Kocaoglu**, **Weihua Gao**, **Ravi S. Jonnal**, and **Donald T. Miller**
Indiana University, School of Optometry, 800 E. Atwater Avenue, Bloomington, Indiana 47405, USA

Abstract

Ultrabroadband sources, such as multiplexed superluminescent diodes (SLDs) and femtosecond lasers, have been successfully employed in adaptive optics optical coherence tomography (AO-OCT) systems for ultrahigh resolution retinal imaging. The large cost differential of these sources, however, motivates the need for a performance comparison. Here, we compare the performance of a Femtolasers Integral Ti:Sapphire laser and a Superlum BroadLighter T840, using the same AO-OCT system and the same subject. In addition, we investigate the capability of our instrument equipped with the Integral to capture volume images of the fovea and adjacent regions on a second subject using the AO to control focus in the retina and custom and freeware image registration software to reduce eye motion artifacts. Monochromatic ocular aberrations were corrected with a woofer-tweeter AO system. Coherence lengths of the Integral and BroadLighter were measured *in vivo* at 3.2 μm and 3.3 μm, respectively. The difference in dynamic range was 5 dB, close to the expected variability of the experiment. Individual cone photoreceptors, retinal capillaries and nerve fiber bundles were distinguished in all three dimensions with both sources. The acquired retinal volumes are provided for viewing in OSA ISP, allowing the reader to data mine at the microscope level.

1. Introduction

Optical coherence tomography (OCT), or time-domain OCT (TD-OCT), is an established non-invasive method for cross-sectional imaging the retina at high axial resolution [1]. Additional improvements in axial resolution have been realized with wider spectral sources (≥100 nm), an advancement coined ultrahigh-resolution OCT (UHR-OCT). UHR-OCT provides an axial resolution of approximately 3 μm in retinal tissue, quantified by the full-width at half maximum (FWHM) coherence length. The higher resolution has enabled clear identification of the major layers of the human retina *in vivo* [2]. In recent years, another variant of OCT—termed spectral-domain OCT (SD-OCT)—has received considerable attention. SD-OCT for retinal imaging was first reported by Wojtkowski *et al.* [3]. It was discovered shortly thereafter to give a ~100-fold improvement in signal-to-noise gain over time-domain OCT [4-6] and could accommodate ultra-broadband sources without loss in sensitivity, both major advantages. *In vivo* imaging of the human retina was demonstrated at video rate with UHR-OCT, operating at an axial resolution of ~3.5 μm [7,8].

While TD-OCT and SD-OCT provide unprecedented axial resolution in the eye, lateral resolution (xy-direction) remains fundamentally limited by the numerical aperture and wave

◊Datasets associated with this article are available at http://hdl.handle.net/10376/1129.

*Corresponding author: E-mail: bcense@indiana.edu.

aberrations of the eye. The former can be minimized by dilating the pupil and imaging with a beam whose size approaches that of the dilated pupil. Defining lateral resolution as $1.22 \cdot \lambda F/d$ (with wavelength λ, focal length F and beam diameter d), a 2.9 μm FWHM airy disk can be achieved at the retina for $\lambda = 840$ nm and d = 6 mm. Such diffraction-limited resolution, however, is possible only if the wave aberrations are negligible, a scenario not found in the human eye.

In the past few years, several groups have successfully corrected for the monochromatic ocular aberrations by integrating adaptive optics (AO) [9] into SD-OCT systems [10-17]. The effectiveness of the correction often depended on the order of the aberration to be corrected. Low-order aberrations (2nd order and less, as for example defocus and astigmatism) in the eye are generally of large magnitude and of low spatial fidelity. Higher-order aberrations (3rd order and above as for example coma and spherical aberration) are generally of small magnitude and of high spatial fidelity. While AO systems for the eye have traditionally relied on a single wavefront corrector for simultaneous correction of both low- and higher-order aberrations, the total aberration content of the eye (including refractive error) and the additional need to focus in the thick retina place high demand on corrector performance. One recent strategy is to distribute the demand across two wavefront correctors using a woofer-tweeter concept. In this arrangement, a large stroke wavefront corrector is cascaded with a high spatial fidelity wavefront corrector for improved correction [15,16,18].

The human eye is also endowed with chromatic aberrations that are significant across the large spectral bandwidth of UHR-OCT light sources. Fernandez *et al.* proposed a customized achromatizing lens to correct the longitudinal chromatic aberrations for UHR-OCT [19]. First UHR-OCT images of the retina with AO, a wide spectral source (≥ 100 nm), and an achromatizing lens were demonstrated by Zawadzki *et al.* [16]. Recently, Fernandez *et al.* reported similar results, using a Ti:Al2O3 (titanium:sapphire) laser with a bandwidth of 140 nm [17].

Both the multiplexed SLDs and the Ti:Al2O3 laser have been evaluated for ultrahigh-resolution AO SD-OCT retinal imaging [16,17]. These instruments have proven successful in imaging the microscopic retina, but the large cost differential between the two sources motivates the need to establish clear tradeoffs between the sources in terms of system performance. These differences, however, are difficult to extract from the current literature given that the sources were evaluated using distinctly different AO SD-OCT instruments and different subjects.

To this end, we compare two commercial broadband sources by integrating both into the same AO SD-OCT instrument (this term will be abbreviated to UHR-AO-OCT in the remainder of the paper) and imaging the fovea of the same subject. The two light sources were a Femtolasers Integral ($\Delta\lambda = 135$ nm, $\lambda_{center} = 800$ nm, P = 60 mW) Ti:Al2O3 laser and a Superlum BroadLighter T840-HP ($\Delta\lambda = 110$ nm, $\lambda_{center} = 840$ nm, P = 12 mW) multiplexed superluminescent diode (SLD). On an additional subject, we investigate the capability of our instrument equipped with the Integral to capture volume images of the fovea and adjacent regions. Acquired volumes are used to compare custom and freeware (an ImageJ plug-in) image registration software for removing eye motion artifacts.

2. Method

Figure 1 shows the layout of the UHR-AO-OCT fiber-based instrument that was used to evaluate the Integral and BroadLighter sources. The BroadLighter was protected by an optical isolator and used in conjunction with HI780 fiber and an 80/20 coupler that optimized system throughput. The Integral was used with SM600 fiber whose cut-off frequency better matched the center wavelength and bandwidth of the source, and preserved the fringe contrast over the

full bandwidth of the Integral. The Integral delivered up to 60 mW of power, which potentially allows use of a 90/10 or 95/5 coupling ratio to increase throughput of the retinal reflection. However in this study, a standard SM600 90/10 coupler (Thorlabs) was found inadequate to couple the full bandwidth of the Integral. A SM600 50/50 coupler proved less lossy and was used instead. Spectra of the two sources measured in the sample arm are given in Fig. 2.

In the sample arm, light was collimated first to a 10 mm beam ($1/e^2$ diameter). Principle components of the sample arm included a Shack-Hartmann wavefront sensor, a Boston Micromachines DM, an AOptix bimorph DM, and two Cambridge Technology galvanometer scanners. All were conjugate to the pupil plane of the subject's eye using relay telescopes consisting of spherical mirrors. The telescopes reduced the beam size entering the eye to 6.0 mm ($1/e^2$ diameter). The total transmission loss of the sample arm (single pass) was 48% as measured with an Ophir broadband power meter. Upon return from the eye, a 90/10 pellicle beam splitter re-directed 10% of the light to the Shack-Hartmann wavefront sensor for AO correction.

During AO operation, the shape of the AOptix DM was optimized first. When best correction was reached—quantified by a stable minimum in the wavefront RMS error—the shape of the AOptix DM was held, and the shape of the BMC DM was then optimized. The BMC mirror was continuously updated at 22.5 Hz during OCT image acquisition. The large stroke of the AOptix mirror was also used to position the focus at two depths in the retina that corresponded to the retinal nerve fiber layer and cone photoreceptors.

Light returning from sample and reference arm was detected by means of a high-speed spectrometer. Light was collimated with a 100 mm achromat, dispersed with a holographic grating (1200 lines per mm) at Littrow angle and focused with a Nikon 135 mm photographic lens. We used a 2048-element (14 μm pixel size) linescan camera from E2V that was run in line trigger (22.5 kHz, $\tau_{integration}$ = 38 μs/ A-scan) and frame trigger (1000 A-scans per frame/ B-scan) mode. The frame trigger was synchronized with the fast galvanometer scanner. The acquisition time for one volume of 100 B-scans was 4.4 s. Based on noise analysis of 1000 acquired spectra [20], the quantum efficiency of the spectrometer was determined at 21 ± 1% for both light sources. Data was acquired through a National Instruments frame grabber (model 1428), while synchronization and scanning waveforms were controlled by two National Instruments I/O boards (model 6052E). Custom control and acquisition software written in C ++ and Python acquired raw data in a circular buffer fashion, such that the last 100 frames of 1000 A-scans each were recorded to hard disk. Data was pre-processed in Matlab, using a calibration method [21] to correctly map data to k-space and compensate for chromatic dispersion.

All procedures on human subjects strictly adhered to the tenets of Helsinki declaration and the Institutional Review Board of Indiana University. Due to limited power from the BroadLighter, the maximum power delivered to the eye was ~400 μW. For the Integral, the power was set at ~525 μW. Both power levels were well within the ANSI standard [22,23]. A headrest and bitebar were used to stabilize the subject's head, and a self-illuminated visual target provided fixation to the same eye that was imaged. Care was taken to maintain a constant optical path length difference between the retinal surface and the zero-delay point for all volumes. In this way, fluctuations in dynamic range due to sensitivity drop-off of the spectrometer were minimized. UHR-AO-OCT volume images were acquired of 3×3 degree (~900 × 900 μm) retinal patches consisting of 100 B-scans of 1000 A-scans each (4.4 s). The spacing between adjacent A-scans in the same B-scan was approximately 0.9 μm, while the spacing between adjacent B-scans was 9 μm. We could not achieve a 0.9 μm spacing between B-scans without creating a data file that was too large for the control software to handle. More importantly, a 0.9 μm spacing in both dimensions of the 3×3 degree field would have increased the acquisition

time by ten times (44 s), a period much too long for subjects to refrain from blinking and to properly fixate. We considered imaging a proportionally smaller patch of retina to preserve the 4.4 s acquisition time, but this would have caused the gross morphology of the foveal pit and large retinal structures of interest to be lost.

Volume images were acquired at 6 degree eccentricity superior and inferior to the foveal center (~1.8 mm). These locations are grossly representative of much of the retina, containing distinct stratification of the major neural layers including a well defined nerve fiber layer, extensive network of retinal capillaries in the plexiform layers, and large cone photoreceptors surrounded by rod photoreceptors. Volume images were also acquired at the foveal center (0 degree eccentricity), the region that provides central vision and is of significant clinical interest. Measurements were performed in the right eyes of three human volunteers. Eyes were dilated and cycloplegia maintained with hourly drops of 0.5% Tropicamide. Volumes were selected for post-processing that exhibited minimal motion artifacts and had diffraction-limited image quality (Strehl > 0.8) as reported by the Shack-Hartmann wavefront sensor. Typically, this meant selecting the best volume out of five volumes acquired. Data from one volunteer was omitted because of a relatively low dynamic range.

After pre-processing in Matlab to correct for dispersion and k-space mapping, data was registered by two different methods. First, custom software written in Matlab and Java automatically aligned adjacent A-scans, after adjustment of several algorithmic variables that optimized the method for a specific dataset. The second method involved the use of ImageJ [24] (National Institute of Health) in conjunction with the plug-in, “StackReg” [25]. Unlike the first, this method is based on freeware that requires no additional software development, requires no adjustment of variables prior to processing a specific dataset, and is straightforward to operate (point-and-click operation).

For the custom software method, A-scans within the same B-scan were positioned axially (in the z-direction) by sliding them relative to their neighbors. The process involved several steps in which A-scans were cross-correlated recursively using different-sized regions of interest until the registered positions stabilized. As an additional step that sometimes was employed and provided some incremental improvement, A-scans were upsampled by four times in the z-direction. Whole B-scans then were registered recursively to one another in the z-direction. Efforts to register in the lateral directions (x-direction and y-direction) were confounded by difficulty separating alignment signals from speckle noise in these axes. As no satisfactory detection scheme was found, registration in the lateral direction was omitted. Finally, the registered datasets were exported from Matlab to OSA ISP via a .MHA file with embedded 3-D metadata. Data was encoded on a log scale using 16-bit precision and the dynamic range was chosen such that the user can adjust the color map to start well below the noise floor.

For the second method, we started by investigating available registration plug-ins for ImageJ to determine which would be most useful for our purpose. “StackReg” and “TurboReg” [25] were determined as potential candidates since they registered frames to a reference frame. Of these, “StackReg” with the “rigid body” setting provided the best performance on our volume data and was selected for comparison with our custom software method. Using ImageJ with the “StackReg” plug-in, 100 pre-processed B-scans in tiff-file format were registered. The registration was constrained in the x-z plane with shift (x- and z-directions) and single-axis rotation within the plane of the B-scan, but did not adjust individual A-scans. The volumes were then cropped to remove empty space at the volume edge, space that was generated by the registration procedures. Data was exported as a single .tif file. The 8-bit precision color map of these files starts just above the noise floor.

3. Results

3.1 Coherence length determination

Figure 3 shows the coherence function of the BroadLighter and Integral, computed as the modulus of the Fourier transform of the measured sample spectra in Fig. 2. The left plot shows the full extent of the coherence function over a ±25 μm range and reveals differences that occur in the sidelobes. For example, the Integral sidelobes are consistently, and often substantially, smaller across the range (except at ±5 μm). The right plot shows the central core of the coherence function (±5 μm range) and reveals differences that occur in the core of the coherence function. For example, the FWHM of the Integral is shown to be 0.7 μm narrower than that of the BroadLighter.

The specular reflection that occurs in the foveal umbo was used as a target for coherence length determination *in vivo* [7,16]. By performing a coherence length measurement on the retina itself, spectral losses in both the system and the eye are included, giving a value that truly represents the coherence length in the retina. In contrast, measurements on a planar mirror and for that matter those in Fig. 3 may not include these losses. Data was zeropadded in k-space by a factor of 10 prior to the Fourier transformation to increase the pixel density in z-space by an order of magnitude. Figure 4 shows the resulting coherence length measurements for the two sources. As shown, the FWHM of the coherence length for the BroadLighter and Integral data was 3.3 ± 0.1 μm and 3.2 ± 0.1 μm, respectively, despite residual chromatic aberration that was not removed completely by the dispersion compensation algorithm (identified by a non-symmetric coherence function).

3.2 Volume data

Figure 5 compares the 3D imaging performance of the BroadLighter (Case 1, Fig. 5 (a)) and Integral (Case 2, Fig. 5 (b)) sources on the same subject. Specifically, two volumes are shown of the foveal pit of the right eye of a 23-old male volunteer. For both volumes, focus was set at the cone photoreceptors using the AOptix DM. The acquired volumes subtended 3 × 3 degrees at the retina, though were reduced somewhat in size (see figure caption) as a consequence of image registration to remove motion artifacts. It is interesting to note that the cone photoreceptors are noticeably sharpest within a ~1.5 degree band of each fast B-scan (x-direction). The location of this band of high image quality varies somewhat across the volumes, but most often appears in the central portion of the fast B-scan. One possible explanation is that the band reflects the eye's isoplanatism, which is often reported at about 1° [26].

Cone photoreceptors provide some of the brightest reflections in the retina. For SD-OCT systems without adaptive optics, the connecting cilia (CC) (interface between the inner and outer segments of the photoreceptor) and the outer tips appear as bright continuous layers (aside from noise generated by speckle). With AO and focus at the photoreceptors, this layer transforms into a highly regular array of individual punctuated spots that exhibit slight (almost random) axial displacements relative to their neighboring spots (see Fig. 6). These punctuated spots are more distinguishable at the connecting cilia (CC) than at the outer tips. From Fig. 6, spacing of the punctuated spots between 0.5 and 1 degree retinal eccentricity is approximately 3 to 4 μm. This is consistent with the spacing of cones at these retinal eccentricities as measured by histology [27] as well as reported in an earlier AO SD-OCT study [13]. Despite the fact that cone photoreceptors are densely packed and small in the acquired volumes (Fig. 5), they can be discerned in almost every B-scan, even as close to the fovea as ~0.5 degrees, demonstrating the ability of the AO system to generate a lateral point spread function that is at least as small as 3 to 4 μm.

Isolated bright reflections in the RPE layer are present in some B-scans and often underlie similar bright reflections at the CC and the outer tips of the photoreceptors (OTPR), an example of which is shown in Fig. 7 (denoted by circles in the 2× magnified inset). Note that the B-scan in Fig. 7 sections the volume in the peripheral fovea (as opposed to the foveal center as given in Fig. 6) where bright reflections in the RPE are found more prevalent. These isolated reflections are likely not the result of random speckle noise, owing to their frequent appearance with similar reflections in the overlying cones. In addition, some extend through adjacent frames (spaced 9 μm apart) and thus are not always circular in shape. Even with the system focus at the photoreceptor layer, capillaries in the plexiform layers were readily observed, albeit likely blurred. For example, small capillaries (~10 μm diameter) are present in OSA ISP X-Z frames #490 to #550 (BroadLighter) and frames #370 to #390 (Integral). On average, the dynamic range of the volume images acquired with the BroadLighter was ~5 dB higher than that with the Integral.

It is important to point out that some reflections in the Fig. 5 volumes appear to axially subtend just 2 μm, which is significantly less than the coherence lengths measured in Fig. 4 (3.2 – 3.3 μm). Specific examples are marked with rectangles in the magnified section of Fig. 7. The apparent discrepancy stems fully from the fact that the coherence length is defined as the FWHM in linear amplitude (Fig. 4), while the retina volumes (Figs. 5 and 6) are displayed in logarithmic intensity, which compresses the perceived extent of single reflections.

Figure 8 shows a volume image of the fovea of a 29-year old female subject. The volume was acquired with the Integral source and with focus at the cone photoreceptor layer. Fewer motion artifacts are evident in this volume compared to the two volumes of Fig. 5, even though the acquisition time was the same (4.4 s). Interestingly, the specular reflection from the base of the foveal pit in this second subject is much broader, 500 μm compared to the 200 μm in the first subject. Individual cone photoreceptors are observed in OSA ISP X-Z frames #197 to #234 (View 1). Faint capillaries are present in numerous OSA ISP X-Z frames about #369 (View 2).

Case 4, Case 5, Case 6, and Case 7 show the four possible combinations of volume images for two retinal locations (6 degrees superior and inferior of the fovea) and two planes of focus (photoreceptor layer and nerve fiber layer), all acquired on the 29-year old female. Figure 9 shows a fundus image of the same eye taken with a commercial scanning laser ophthalmoscope (SLO). The two UHR-AO-OCT volume images—depicted by corresponding C-scan slices through the nerve fiber layer—are shown properly scaled and superimposed on the fundus image. Note the strong correspondence in the vasculature pattern between the C-scan images and the SLO fundus image. This strong correspondence confirms the actual location of the volume images and supports the integrity of the UHR-AO-OCT data at least at the macroscopic level. Also shown in the figure is an oblique B-scan extracted from the volumetric image (Case 7). To reduce the influence of speckle noise, two adjacent oblique B-scans were averaged. Individual nerve fiber bundles are clearly discernable in the B-scan, one bundle with a diameter of 40 μm is labeled. The bundles are also present in the mirror volume taken 6 degrees inferior of the fovea. At both locations, the orientation and path of the bundles are clear, arcing slightly around the fovea.

While the 6 degree superior volume was acquired with the fast B-scan perpendicular to the nerve fiber bundles (vertical fast scan in Fig. 9), the inferior volume was acquired with a fast B-scan parallel to the bundles (horizontal fast scan in Fig. 9). As evident from Case 4 and Case 5, fast B-scans parallel to the bundles are less favorable at revealing their pattern and orientation, likely because the high spatial frequency information of the bundles is sampled much more coarsely, both spatially (9 μm instead of 0.9 μm) and temporally (44 ms instead of 44 μs).

In the four volumes of Fig. 10, all major retinal layers (RNFL, GCL, IPL, INL, OPL, ONL, CC, OTPR, and RPE) as well as some choroid (C) are clearly discernible even though the plane of focus was optimal for only one or two layers. For these volumes, custom software was used to align adjacent A-scans and B-scans. Major retinal vasculature is clearly visible in the volumes whether displayed volumetrically or cross-sectionally (B-scan and C-scan). The smaller retinal capillaries straddling the plexiform layers are also visible in both B-scans and C-scans, though their intricate pattern is most pronounced in the latter. Volume images acquired with focus at the RNFL reveal individual nerve fiber bundles that are readily distinguishable in both B-scan and C-scan slices. In the C-scans, the orientation and pattern of the nerve fiber bundles as they traverse across the retinal surface can be appreciated. In volume images with focus at the cone photoreceptors, individual cones are present in both B-scans and C-scans. Following individual cones through C-scan sections of the volumes reveals essentially the same cone mosaic pattern at the CC and OTPR layers. This observation is consistent with our earlier findings [13].

The volumetric data sets in this paper can be analyzed in the OSA ISP software by the reader, but OSA ISP also offers the option to output volumetric data as a movie file. Figure 11 contains a movie that was generated in OSA ISP, showing a volumetric dataset taken superior to the fovea (Case 7). In this movie, the tilted volume is first rotated 360°. Retinal nerve fiber bundles can be seen at the top of the retina and the shadow of large blood vessels readily apparent at the bottom. In the final segment of the video, the retina slightly rotates and enlarges, zooming in on the retinal nerve fiber layer bundles. The color map was adjusted to enhance contrast of the nerve fiber bundles.

5. Discussion

5.1 Performance of the BroadLighter and the Integral broadband sources

For retinal imaging, the Femtolasers Integral offers more power and a somewhat wider, smoother, and better positioned (blue shifted) spectrum than the Superlum BroadLighter. The Integral is also significantly more expensive.

By Fourier transforming the spectra as measured in the sample arm, the coherence length of the Integral and BroadLighter was estimated at 2.1 μm and 2.8 μm (n = 1.38), respectively. *In vivo* measurements using the specular reflection from the base of the foveal pit yielded values of 3.2 ± 0.1 μm and 3.3 ± 0.1 μm, respectively, which are noticeably higher than that predicted by the Fourier transform approach. The fact that the two sources produced strikingly similar *in vivo* coherence lengths with one being much longer than the corresponding Fourier transform estimate suggests that other factors might be limiting resolution. These include spectral losses in the eye and OCT system, and imperfect dispersion compensation. While these additional factors were carefully accounted for in the experiment, even better control may be necessary to fully tap the spectral content of these sources, especially the Integral. With the same eye in the system, volume images of the foveal pit were acquired with both light sources. The specular reflection from the base of the foveal pit revealed more pronounced sidelobes in the axial PSF (Fig. 4) for the BroadLighter than for the Integral. This is consistent with the smoother, more Gaussian spectrum of the Integral. Sidelobes are undesirable as they reduce image contrast and enhance speckle noise.

The dynamic range of images collected on the same volunteer with the Integral was about 5 dB less than that of the BroadLighter. This difference cannot be attributed to the performance of the spectrometer since it was calibrated to be equal for both sources. Furthermore, a noise analysis of the system using 1000 acquired spectra revealed that the instrument operates in the shot noise limit regardless of the source [20]. Consistent with that, the noise floor in the two datasets (Fig. 5) is exactly the same. In addition, the fine details that can be seen in both datasets

of Fig. 5 of the cone photoreceptor layer demonstrate that the adaptive optics effectively reduced the aberrations, and in fact the Shack-Hartmann measurements taken during data acquisition reported diffraction-limited performance for both. Part of the 5 dB drop in dynamic range could be attributed to the different fiber coupling ratios (80/20 and 50/50), a difference of ~2dB. This difference, however, is mostly offset by the extra 125 μW of the Integral (+ ~25%; + ~1.2 dB). Together, these hardware differences (2 dB − 1.2 dB = ~0.8 dB) fall noticeably short of the 5 dB difference. An explanation could lie in the fact that the images obtained with the two sources, albeit from the same volunteer, were taken on different days and at different times. For example, images with the BroadLighter (Fig. 5) were taken in the morning, while those with the Integral (also Fig. 5) were taken in the evening days later. Any temporal variations in the eye's optical quality and clarity (e.g., integrity of the pre-corneal tear film) beyond which are correctable by the AO and on a time scale similar to the separation of the measurements (days) would have contributed to a false difference in source performance. While we do not know what this difference was, we have some appreciation for what it might be based on the variations measured in individual sessions (~2 hours). For example, the variation in dynamic range over a single session was typically about 2 to 4 dB. Note that the design of the experiment largely avoided this short term variation by the manner in which the best volumes were selected. However, the presence of similar variations across days would not have been avoided. Based on this assessment, a more accurate comparison of the two sources would require comparing datasets that are averaged over several days or even weeks.

Regardless of the origins for the 5 dB shortfall, more than half of it can be recovered by using the Integral with a 95/5 fiber coupler (as opposed to the 50/50 used), made possible by the extra power that the Integral offers. In theory, switching fiber couplers from 50/50 to 95/5 increases the sensitivity by 2.7 dB. Another benefit of the Integral is that its blue-shifted spectrum is more sensitive to CCD-based Shack-Hartmann wavefront sensors, an advantage if the same source is used for OCT imaging and wavefront sensing.

5.2 Reflecting structures below cone photoreceptors

Images acquired with the UHR-AO-OCT system often show bright, isolated reflections in the RPE layer, as for example the B-scan in Fig. 7. The OSA ISP software allows determination of the depth of these reflections, as for example relative to the outer tips of the photoreceptor layer. Doing so on 50 such bright reflections that were selected in multiple B-scans (with the one caveat that they fell below an overlying, distinguishable cone so as to measure the depth) revealed a bimodal depth distribution. The average distance of the first peak from the outer tips of the photoreceptors was 15 ± 2 μm. The average distance of the second peak was 22 ± 4 μm. These distances when compared to conventional anatomy of the retina suggest that the bright reflections may straddle the monolayer of RPE cells with the first originating near the anterior portion of the RPE cells and the latter originating below the RPE, perhaps from Bruch's membrane [28,29].

In some B-scans of the 23-year old male (Case 1 and Case 2), very narrow columns of relatively higher reflective tissue can be seen starting at the RPE layer and extending more than 250 μm deep into the choroid (Case 1: OSA ISP X-Y frame #35, View 3). These columns—not observed in the other subject—are nominally less than 10 μm wide and often characterized by a bright reflection at Bruch's membrane (i.e., the second reflection of the bimodal distribution discussed above). It may be that the normal absorptive properties (e.g., melanin) of the RPE are diminished in these cells thus allowing the broadband light to pass through the RPE layer and illuminate the underlying layers in the choroid. A close inspection of C-scans through the same volume did not reveal any additional clues on the origin of these bright columns.

5.3 Performance of the registration software

Of the seven volume datasets presented, three (Case 1, Case 2, and Case 3) were registered using the "StackReg" registration plug-in for ImageJ and four (Case 4, Case 5, Case 6, and Case 7) with custom software. Comparison of these for registration correctness, however, is hampered by differences in the subjects, retinal locations, light sources, and plane of focus used. To avoid these unwanted sources of error and thus provide a direct comparison of the registration performance, Fig. 12 shows a side-by-side comparison of representative registration outcomes using the same volume dataset (Case 7). C-scans in the figure were extracted at the same depth in the RNFL using OSA ISP. As apparent in the figure, the C-scan registered with ImageJ is notably reduced in the vertical direction due to cropping, a consequence of significant B-scan re-alignment in the opposite orientation. It appears that the "StackReg" plug-in for ImageJ was overly sensitive to the large, highly reflective vessel that diagonally traverses the volume (confirmed with the SLO fundus image), thus over shifting the B-scans so as to re-align the blood vessel horizontally. The custom software did not share this problem as it permits user-defined regions of interests that can be strategically defined to avoid retinal structures (such as blood vessels) that compromise the registration process. Note the SLO fundus image was acquired after the custom registration was applied to this case and therefore had no influence on the registration outcome. Also apparent in the figure, the striation pattern of the nerve fiber bundles is significantly less distinguishable with the "StackReg" plug-in as compared to with the custom software. Again this points to reduced accuracy with the plug-in. On the flip side, ImageJ proved much less labor intensive, required no programming experience and was quickly applied with little preparation, major advantages especially when volumes need to be inspected quickly.

6. Conclusion

We have compared two ultrabroadband sources, a Femtolasers Integral and a Superlum BroadLighter, using essentially the same UHR-AO-OCT system and same subject. Based on spectral measurements in the sample arm at the location of the eye, the coherence lengths of these two sources should nominally correspond to 2.1 μm and 2.8 μm, respectively, assuming an index of refraction of 1.38. Measurements in the fovea yield values of 3.2 ± 0.1 μm and 3.3 ± 0.1 μm, respectively. The difference between these measurements is attributed to spectral losses in the eye and OCT system, and imperfect dispersion compensation. Dynamic range with the BroadLighter was found to be 5 dB higher, close to the expected variability of the experiment.

By focusing the AOptix DM at different depths in the retina, individual cone photoreceptors, retinal capillaries and nerve fiber bundles were distinguished. These volumes also gave rise to speculation about structures that can be seen within individual cone outer segments and immediately beneath the cone photoreceptor layer. Further experiments are needed to elicit the origin of these apparent structures. The vasculature pattern in volumetric datasets acquired at 6° retinal eccentricity (superior and inferior) demonstrated strong correspondence with a clinical SLO image on the same eye. This confirmed the actual location of the volume images and supported the integrity of the UHR-AO-OCT data, at least at the macroscopic level. At the microscopic level, focus at the nerve fiber layer permitted clear observation of the three-dimensional structure of individual nerve fiber bundles. In a comparison of two image registration algorithms used to remove motion artifacts, the "StackReg" registration plug-in for ImageJ was easier to implement and use, but our own registration software provided superior registration

Acknowledgments

The authors thank the subjects who volunteered for this study. They also thank Robert Zawadzki and John Werner (UC Davis), Steve Jones and Julia Evans (Laurence Livermore National Lab) for fruitful discussions about optical coherence tomography and adaptive optics. We thank Toco Chui for taking the SLO image and Daniel Jackson and William Monette for machining and electronic support. Financial support was provided by the National Eye Institute grants 5R01 EY014743 and 1R01 EY018339. This work was also supported in part by the National Science Foundation Science and Technology Center for Adaptive Optics, managed by the University of California at Santa Cruz under cooperative agreement No. AST-9876783.

References and Links

1. Huang D, Swanson EA, Lin CP, Schuman JS, Stinson WG, Chang W, Hee MR, Flotte T, Gregory K, Puliafito CA, Fujimoto JG. Optical coherence tomography. Science 1991;254:1178–1181. [PubMed: 1957169]
2. Drexler W, Morgner U, Ghanta RK, Kartner FX, Schuman JS, Fujimoto JG. Ultrahigh-resolution ophthalmic optical coherence tomography. Nat Med 2001;7:502–507. [PubMed: 11283681]
3. Wojtkowski M, Leitgeb R, Kowalczyk A, Bajraszewski T, Fercher AF. In vivo human retinal imaging by Fourier domain optical coherence tomography. J Biomed Opt 2002;7:457–463. [PubMed: 12175297]
4. Mitsui T. Dynamic range of optical reflectometry with spectral interferometry. Jpn J Appl Phys 1999;38 (Part 1):6133–6137.
5. Leitgeb R, Hitzenberger CK, Fercher AF. Performance of fourier domain vs. time domain optical coherence tomography. Opt Express 2003;11:889–894. [PubMed: 19461802]
6. de Boer JF, Cense B, Park BH, Pierce MC, Tearney GJ, Bouma BE. Improved signal-to-noise ratio in spectral-domain compared with time-domain optical coherence tomography. Opt Lett 2003;28:2067–2069. [PubMed: 14587817]
7. Cense B, Nassif NA, Chen TC, Pierce MC, Yun SH, Park BH, Bouma BE, Tearney GJ, de Boer JF. Ultrahigh-resolution high-speed retinal imaging using spectral-domain optical coherence tomography. Opt Express 2004;12:2435–2447. [PubMed: 19475080]
8. Wojtkowski M, Srinivasan VJ, Ko TH, Fujimoto JG, Kowalczyk A, Duker JS. Ultrahigh-resolution, high-speed, Fourier domain optical coherence tomography and methods for dispersion compensation. Opt Express 2004;12:2404–2422. [PubMed: 19475077]
9. Porter, J.; Queener, H.; Lin, J.; Thorn, KE.; Awwal, A. Adaptive Optics for Vision Science: Principles, Practices, Design and Applications. Wiley; 2006.
10. Zhang Y, Rha JT, Jonnal RS, Miller DT. Adaptive optics parallel spectral domain optical coherence tomography for imaging the living retina. Opt Express 2005;13:4792–4811. [PubMed: 19495398]
11. Zawadzki RJ, Jones SM, Olivier SS, Zhao MT, Bower BA, Izatt JA, Choi S, Laut S, Werner JS. Adaptive-optics optical coherence tomography for high-resolution and high-speed 3D retinal in vivo imaging. Opt Express 2005;13:8532–8546. [PubMed: 19096728]
12. Fernandez EJ, Povazay B, Hermann B, Unterhuber A, Sattmann H, Prieto PM, Leitgeb R, Ahnelt P, Artal P, Drexler W. Three-dimensional adaptive optics ultrahigh-resolution optical coherence tomography using a liquid crystal spatial light modulator. Vision Res 2005;45:3432–3444. [PubMed: 16249013]
13. Zhang Y, Cense B, Rha J, Jonnal RS, Gao W, Zawadzki RJ, Werner JS, Jones S, Olivier S, Miller DT. High-speed volumetric imaging of cone photoreceptors with adaptive optics spectral-domain optical coherence tomography. Opt Express 2006;14:4380–4394. [PubMed: 19096730]
14. Bigelow CE, Iftimia NV, Ferguson RD, Ustun TE, Bloom B, Hammer DX. Compact multimodal adaptive-optics spectral-domain optical coherence tomography instrument for retinal imaging. J Opt Soc Am A 2007;24:1327–1336.
15. Zawadzki RJ, Choi SS, Jones SM, Oliver SS, Werner JS. Adaptive optics-optical coherence tomography: optimizing visualization of microscopic retinal structures in three dimensions. J Opt Soc Am A 2007;24:1373–1383.

16. Zawadzki RJ, Cense B, Zhang Y, Choi SS, Miller DT, Werner JS. Ultrahigh-resolution optical coherence tomography with monochromatic and chromatic aberration correction. Opt Express 2008;16:8126–8143. [PubMed: 18545525]

17. Fernandez EJ, Hermann B, Povazay B, Unterhuber A, Sattmann H, Hofer B, Ahnelt PK, Drexler W. Ultrahigh resolution optical coherence tomography and pancorrection for cellular imaging of the living human retina. Opt Express 2008;16:11083–11094. [PubMed: 18648422]

18. Chen DC, Jones SM, Silva DA, Olivier SS. High-resolution adaptive optics scanning laser ophthalmoscope with dual deformable mirrors. J Opt Soc Am A 2007;24:1305–1312.

19. Fernandez EJ, Vabre L, Hermann B, Unterhuber A, Povazay B, Drexler W. Adaptive optics with a magnetic deformable mirror: applications in the human eye. Opt Express 2006;14:8900–8917. [PubMed: 19529270]

20. Nassif NA, Cense B, Park BH, Pierce MC, Yun SH, Bouma BE, Tearney GJ, Chen TC, de Boer JF. In vivo high-resolution video-rate spectral-domain optical coherence tomography of the human retina and optic nerve. Opt Express 2004;12:367–376. [PubMed: 19474832]

21. Mujat M, Park BH, Cense B, Chen TC, de Boer JF. Autocalibration of spectral-domain optical coherence tomography spectrometers for in vivo quantitative retinal nerve fiber layer birefringence determination. J Biomed l Opt 2007;12:041205.

22. Delori FC, Webb RH, Sliney DH. Maximum permissible exposures for ocular safety (ANSI 2000), with emphasis on ophthalmic devices. J Opt Soc Am A 2007;24:1250–1265.

23. A.N.S.I.. Z136.1 Safe use of lasers. Laser Institute of America; 2007.

24. Abramoff MD, Magalhaes PJ, Ram SJ. Image processing with ImageJ. Biophotonics Int 2004;11:36–43.

25. Thevenaz P, Ruttimann UE, Unser M. A pyramid approach to subpixel registration based on intensity. IEEE Trans Image Process 1998;7:27–41. [PubMed: 18267377]

26. Bedggood P, Daaboul M, Ashman R, Smith G, Metha A. Characteristics of the human isoplanatic patch and implications for adaptive optics retinal imaging. J Biomed Opt 2008;13:024008. [PubMed: 18465971]

27. Curcio CA, Sloan KR, Kalina RE, Hendrickson AE. Human photoreceptor topography. J Comp Neurol 1990;292:497–523. [PubMed: 2324310]

28. Bloom, W.; Fawcett, DW. A Textbook of Histology. W.B. Saunders Company; 1975.

29. Hogan, MJ.; Alvarado, JA.; Esperson Weddell, J. Histology of the Human Eye. W.B. Saunders Company; 1971.

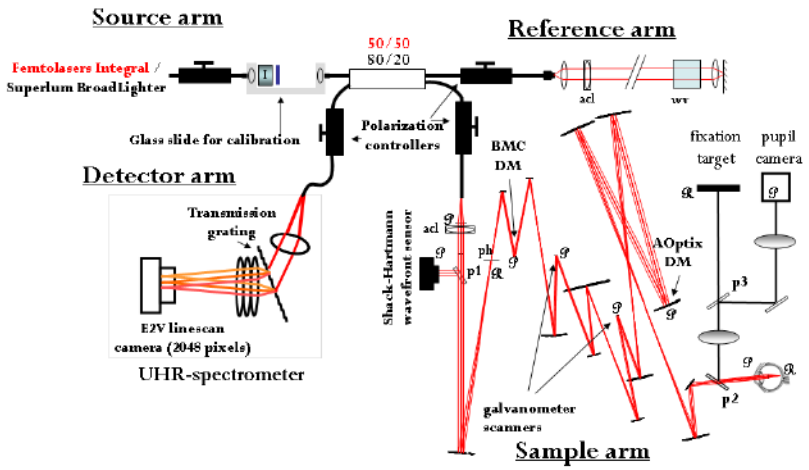

Fig. 1.

Schematic of the UHR-AO-OCT system for retinal imaging. The sample arm contains a woofer-tweeter AO system for correction of ocular monochromatic aberrations. The AO cascades an AOptix deformable mirror (DM) (36 electrodes; 16 μm stroke) for correction primarily of lower-order aberrations and a Boston MicroMachines Corporation (BMC) DM (140 actuators; 3.8 μm stroke) for correction primarily of higher-order aberrations. Unlike previous woofer-tweeter systems for the eye, the AOptix DM is strategically positioned close to the eye to prevent beam distortion when large low-order aberrations are present in the eye [13]. Wavefront measurements are obtained with a Shack-Hartmann wavefront sensor (20×20 lenslet array). A customized achromatizing lens (acl) was introduced in the beam path directly behind the fiber collimator in the sample arm for correction of ocular chromatic aberrations. A similar lens was placed in the reference arm to compensate for dispersion of the former. A single glass slide (0.24 mm thick) was used in the source arm for calibrating the SD-OCT system. The Superlum BroadLighter was used with HI780 fiber, an 80/20 coupler, and an optical isolator. The Femtolasers Integral was used with SM600 fiber, a 50/50 coupler, and no isolator. Key: I: isolator; p1-p3: pellicle beamsplitters; ph: pinhole; acl: custom achromatizing lens; wv: water vial for balancing the chromatic dispersion of the eye; P/R: pupil and retina conjugate planes. Footprint of the instrument is ~2.5′×4′.

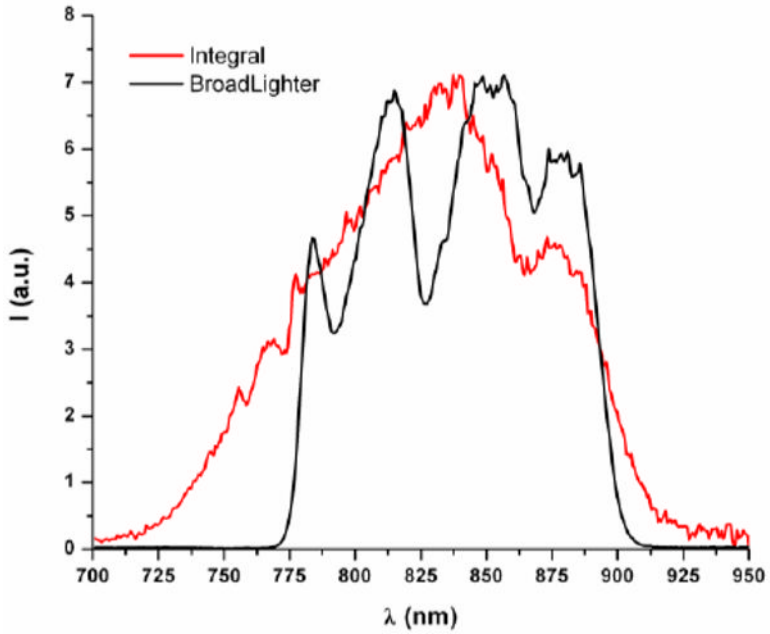

Fig. 2.

Integral and BroadLighter spectra measured in the sample arm. Measurements were acquired at the end of the sample arm at the location of the eye. The FWHM of the Integral (red) and BroadLighter (black) spectra are approximately 120 nm and 110 nm, respectively. Overall spectral shape of the Integral is significantly more Gaussian than that of the BroadLighter. Note that the full 135 nm bandwidth of the Integral did not reach the location of the eye, likely due to spectral losses in the SM600 fiber and sample arm.

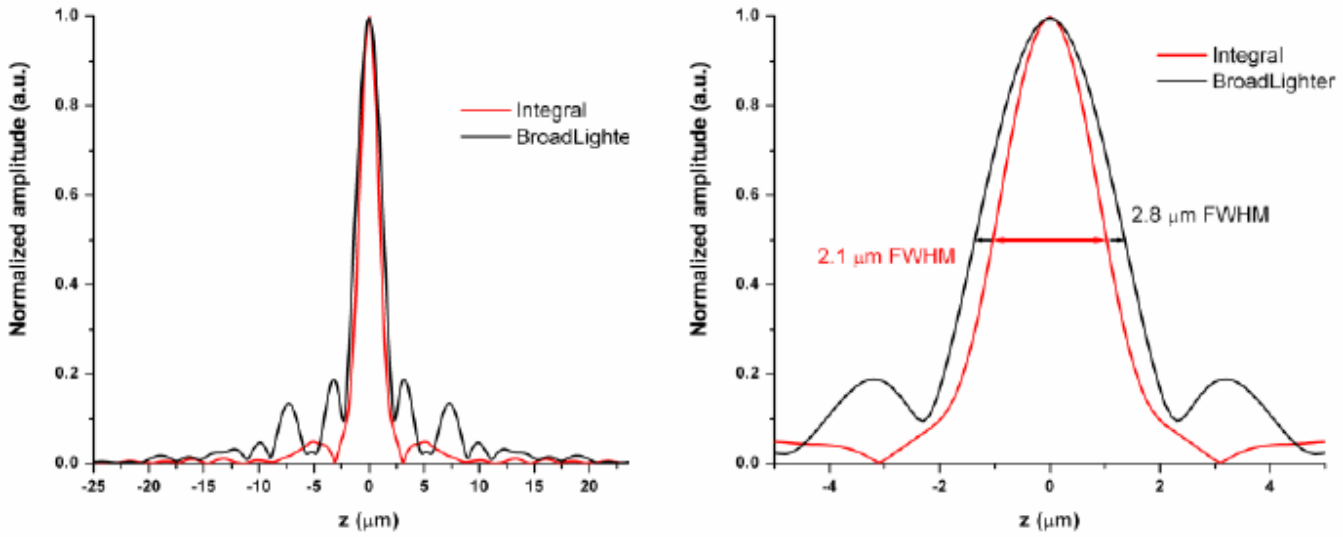

Fig. 3.

Normalized coherence functions calculated from the BroadLighter (black line) and Integral (red line) spectra of Fig. 2. A refractive index of 1.38 for retinal tissue is assumed.

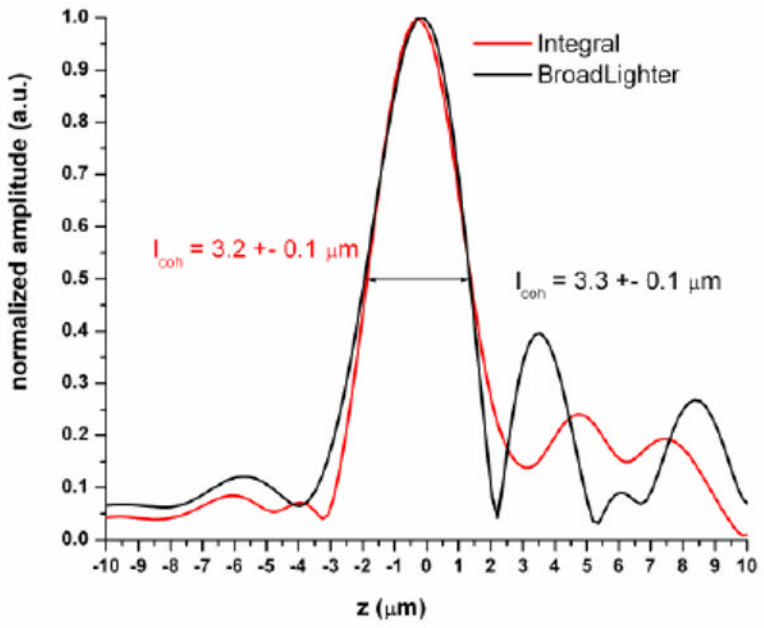

Fig. 4.
Normalized coherence functions of the BroadLighter (black line) and Integral (red line) sources using the specular reflection from the foveal umbo.

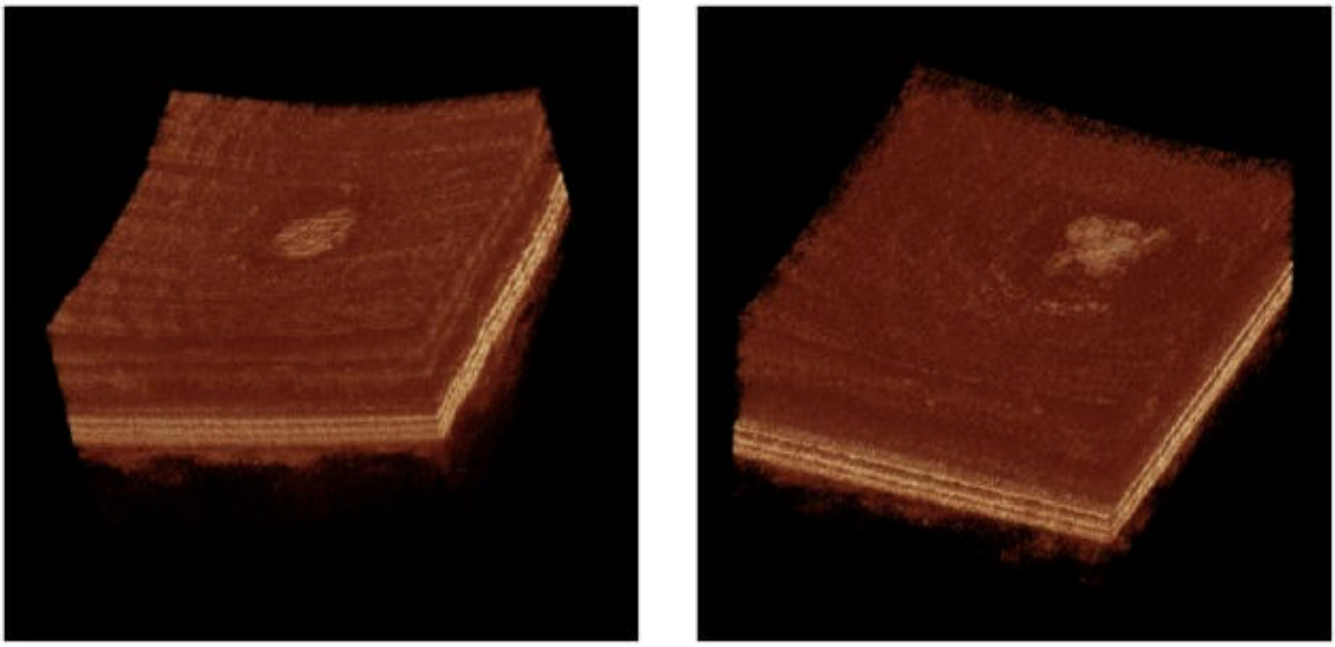

Fig. 5.
UHR-AO-OCT volume images of the foveal pit in the same subject, a 23-year old male, using the (a) BroadLighter (Case 1) and (b) Integral (Case 2) light sources. Dimensions of the BroadLighter volume are 879 × 100 × 717 voxels (width × length × depth) that correspond to 791 × 900 × 645 μm. Dimensions of the Integral volume are 747 × 100 × 559 voxels (width × length × depth) that correspond to 673 × 900 × 503 μm. The specular reflection visible in the central fovea is approximately 200 μm in diameter. Focus of the UHR-AO-OCT instrument was positioned at the photoreceptor layer using the AOptix DM. Adjacent B-scans were realigned using the “StackReg” registration plug-in for ImageJ.

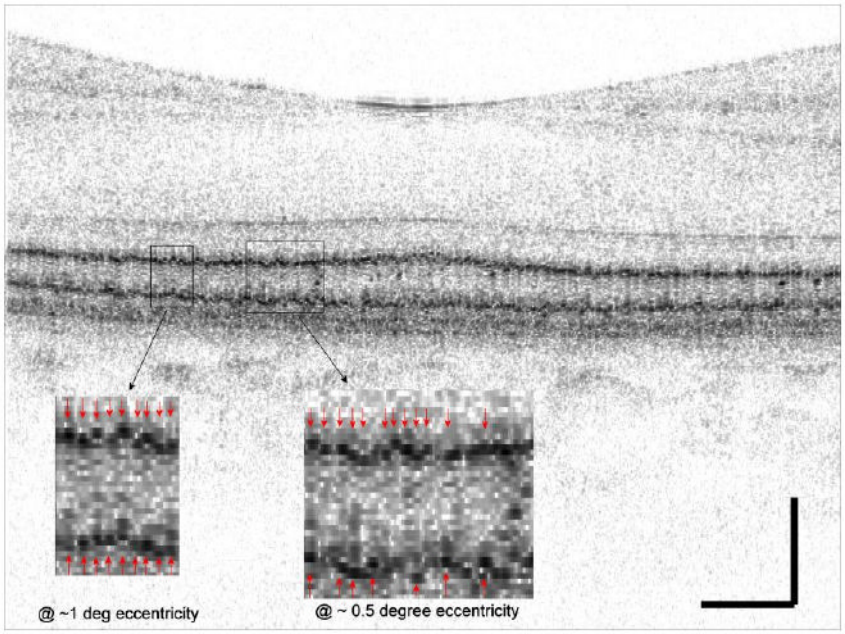

Fig. 6.

UHR-AO-OCT fast B-scan (inverted gray-scale) of the foveal pit of a 23-year old male obtained with the BroadLighter light source, extracted from Fig. 5 (Case 1). Scale bars indicate 100 μm. Arrows in the 3× magnified insets demark reflections from the connecting cilia and the outer photoreceptor tips that are suggestive of individual cone photoreceptors.

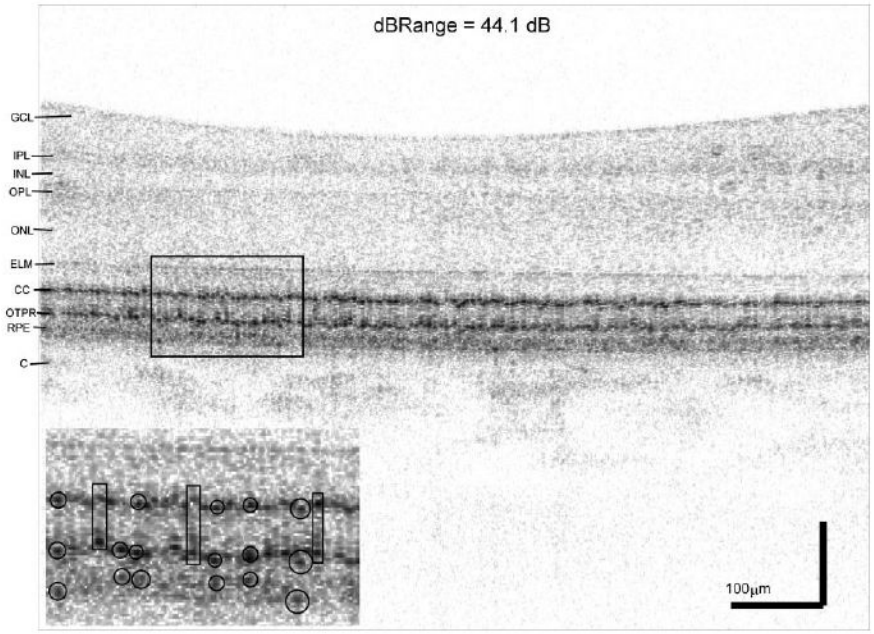

Fig. 7.

B-scan image extracted from the BroadLighter volume in Fig. 5 (Case 1). Data was encoded over 44 dB above the noise floor and displayed using an inverted gray scale. Note the uneven appearance of the CC that is particularly evident in the 2× magnified view (inset), which shows a highlighted rectangular region at the depth of the photoreceptors. Multiple reflections sometimes occur in the same outer segment (denoted by rectangles in the inset). Also in the inset, the strongest reflections from within the RPE often coincide with reflections from an overlying cone (denoted by circles in the inset). GCL: ganglion cell layer; IPL: inner plexiform layer; INL: inner nuclear layer; OPL: outer plexiform layer; ONL: outer nuclear layer; ELM: external limiting membrane; CC: connecting cilia; OTPR: outer tips of the photoreceptors; RPE: retinal pigment epithelium; C: choroid.

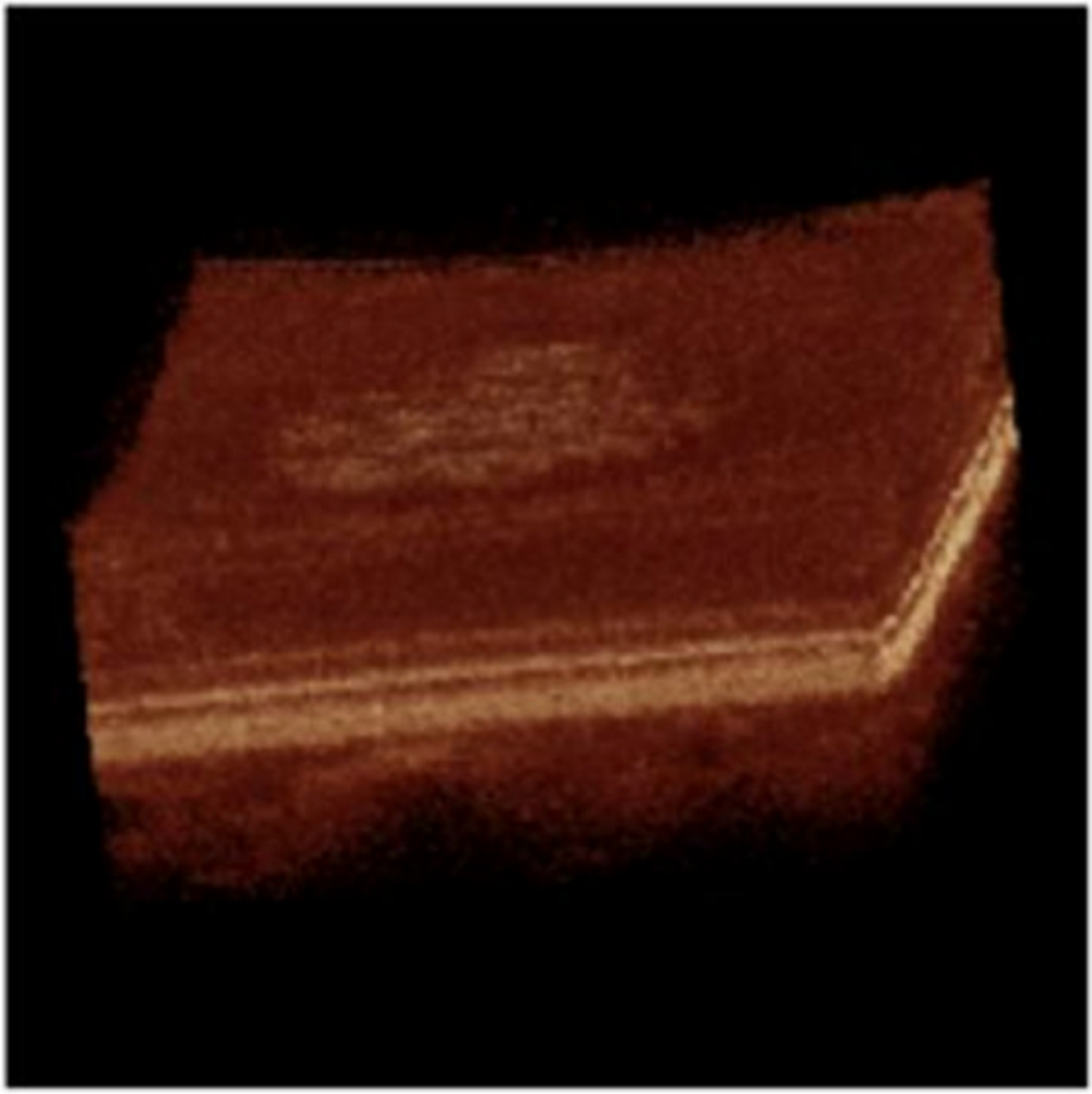

Fig. 8.
UHR-AO-OCT volume image of the foveal pit of a 29-year old female obtained with the Integral source (Case 3). Volume dimensions are 878 × 100 × 485 voxels (width × length × depth) that correspond to 790 × 900 × 436 μm. The specular reflection visible in the center of the fovea is approximately 500 μm in diameter. Focus of the UHR-AO-OCT instrument was positioned at the photoreceptor layer using the AOptix DM. Adjacent B-scans were realigned using the “StackReg” registration plug-in for ImageJ.

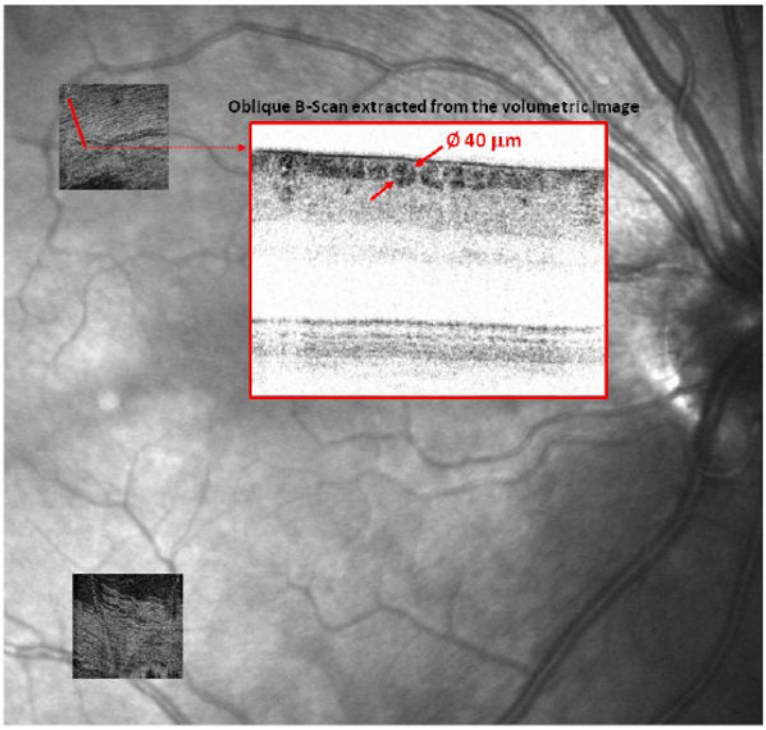

Fig. 9.

C-scans of Case 5 and Case 7 superimposed on a commercial SLO fundus image taken from the same 29-year old female subject. Both C-scans slice through the RNFL and show large blood vessels that lie at the same proximal depth. (inset) B-scan is an average of two adjacent oblique B-scans extracted from the Case 7 volume. An individual nerve fiber bundle is highlighted whose diameter was measured at 40 µm. Other bundles of similar size are also present.

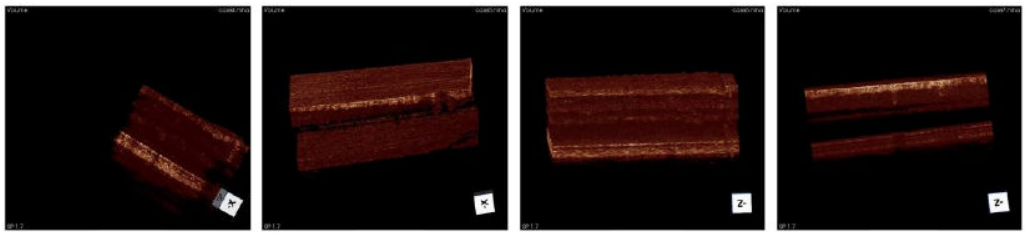

Fig. 10.
UHR-AO-OCT volume images representing the four possible combinations of two retinal locations and two planes of focus, all acquired on the same subject with the Integral source. Retinal locations are (a), (b) 6 degree inferior (Case 4 and Case 5, respectively) and (c), (d) superior (Case 6 and Case 7, respectively) of the fovea. Focus was positioned at the photoreceptor (Case 4 and Case 6) and nerve fiber (Case 5 and Case 7) layers. Custom registration software was used to align adjacent A-scans and B-scans. Subject was a 29-year old female.

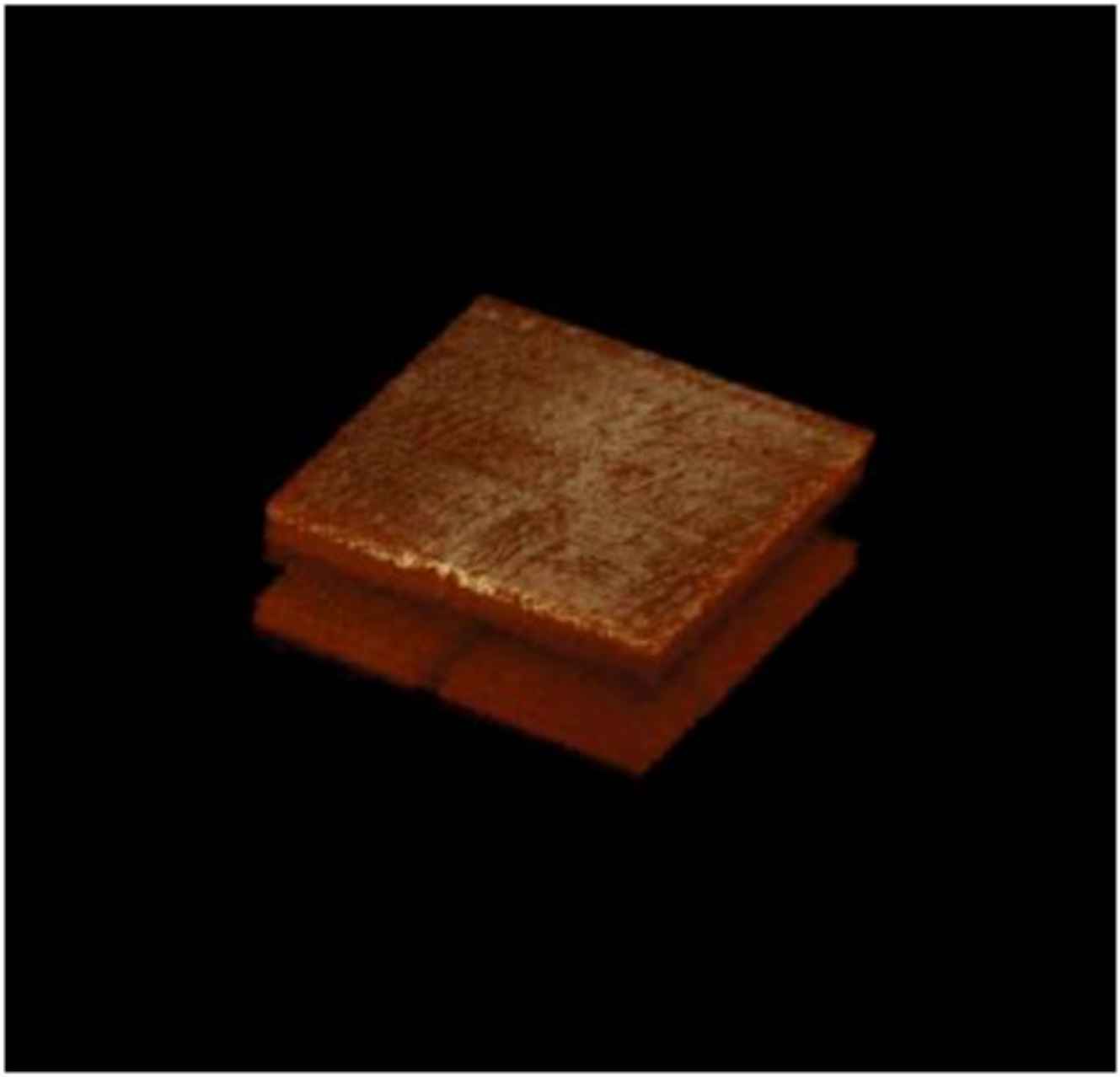

Fig. 11.
Rotating volumetric data set acquired at 6 degrees superior of the fovea of a 29-year old female with focus at the nerve fiber layer (Media 1).

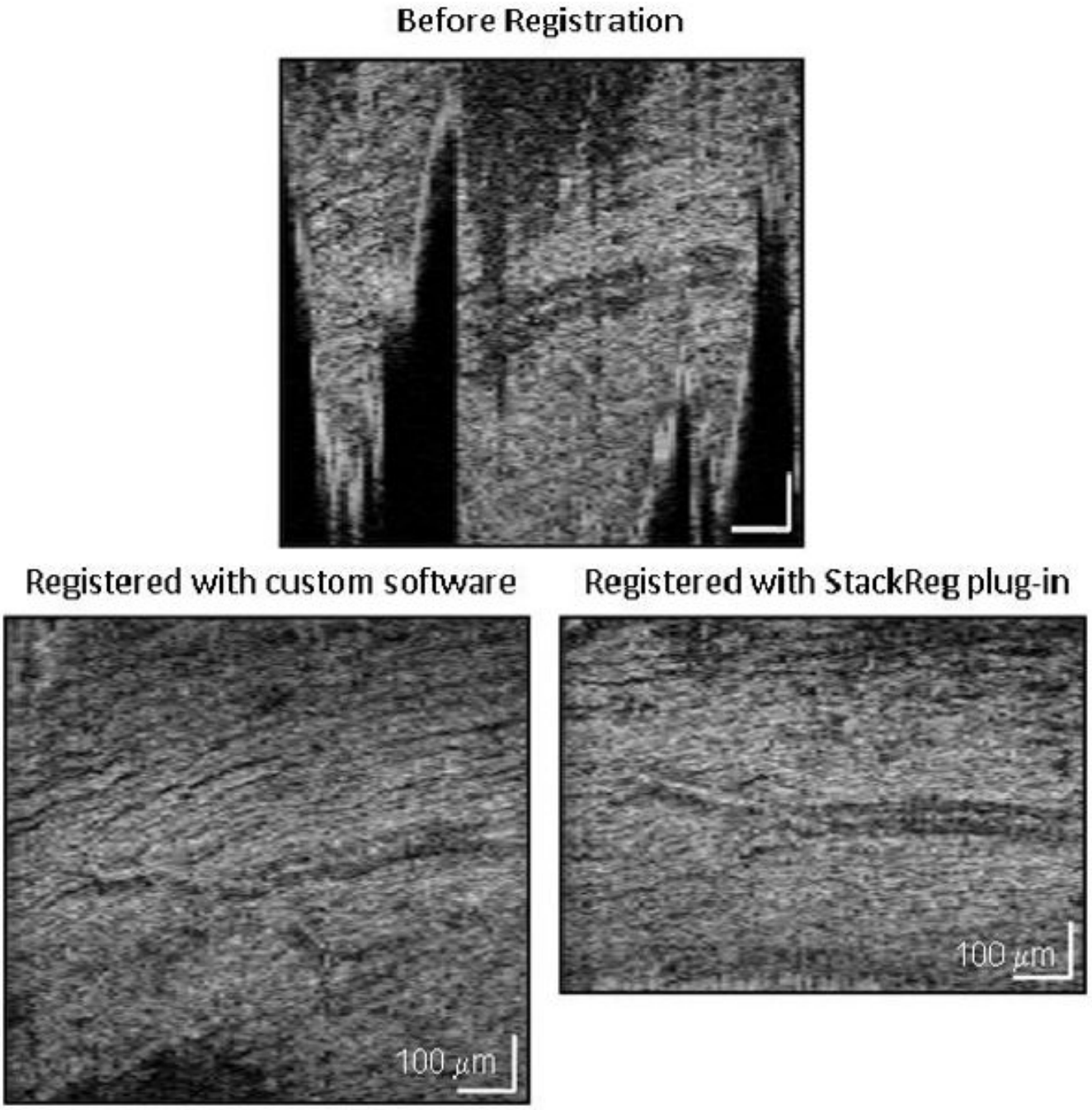

Fig. 12.

Performance of volume registration software using the “same” C-scan extracted from Case 7: (top) unregistered, (left) registered with custom software, and (right) registered using the “StackReg” plug-in for ImageJ. The C-scan slices through the nerve fiber layer. The volume was acquired at 6 degrees superior of the fovea with focus at the nerve fiber layer. Note the dark regions in the unregistered C-scan correspond to the vitreous and are due to axial motion of the eye during the volume acquisition. White scale bars indicate a length of 100 μm.